Small-molecule Ca$_V\alpha_1$·Ca$_V\beta$ antagonist suppresses neuronal voltage-gated calcium-channel trafficking

Xingjuan Chen[a,1], Degang Liu[b,1], Donghui Zhou[b], Yubing Si[b], David Xu[c,d], Christopher W. Stamatkin[a,b], Mona K. Ghozayel[b], Matthew S. Ripsch[e], Alexander G. Obukhov[a,f,2], Fletcher A. White[e,f,2], and Samy O. Meroueh[b,c,f,2]

[a]Department of Cellular and Integrative Physiology, Indiana University School of Medicine, Indianapolis, IN 46202; [b]Department of Biochemistry and Molecular Biology, Indiana University School of Medicine, Indianapolis, IN 46202; [c]Center for Computational Biology and Bioinformatics, Indiana University School of Medicine, Indianapolis, IN 46202; [d]Department of BioHealth Informatics, Indiana University School of Medicine, Indianapolis, IN 46202; [e]Department of Anesthesia, Indiana University School of Medicine, Indianapolis, IN 46202; and [f]Stark Neurosciences Research Institute, Indiana University School of Medicine, Indianapolis, IN 46202

Extracellular calcium flow through neuronal voltage-gated Ca$_V$2.2 calcium channels converts action potential-encoded information to the release of pronociceptive neurotransmitters in the dorsal horn of the spinal cord, culminating in excitation of the postsynaptic central nociceptive neurons. The Ca$_V$2.2 channel is composed of a pore-forming α_1 subunit (Ca$_V\alpha_1$) that is engaged in protein–protein interactions with auxiliary α_2/δ and β subunits. The high-affinity Ca$_V$2.2α_1·Ca$_V\beta_3$ protein–protein interaction is essential for proper trafficking of Ca$_V$2.2 channels to the plasma membrane. Here, structure-based computational screening led to small molecules that disrupt the Ca$_V$2.2α_1·Ca$_V\beta_3$ protein–protein interaction. The binding mode of these compounds reveals that three substituents closely mimic the side chains of hot-spot residues located on the α-helix of Ca$_V$2.2α_1. Site-directed mutagenesis confirmed the critical nature of a salt-bridge interaction between the compounds and Ca$_V\beta_3$ Arg-307. In cells, compounds decreased trafficking of Ca$_V$2.2 channels to the plasma membrane and modulated the functions of the channel. In a rodent neuropathic pain model, the compounds suppressed pain responses. Small-molecule α-helical mimetics targeting ion channel protein–protein interactions may represent a strategy for developing nonopioid analgesia and for treatment of other neurological disorders associated with calcium-channel trafficking.

calcium channel | protein–protein interactions | small-molecule inhibitors | pain | β subunit

In the central nervous system, voltage-gated calcium channels (Ca$_V$s) play important and diverse roles in the synaptic transmission of electrical signals (e.g., neurotransmitter release), in the integration and modulation of these signals, and in the transduction of membrane depolarization into intracellular signals (1). To accomplish these diverse functions, neurons express a variety of calcium channels that are composed of large heteromeric assemblies of pore-forming α_1 (Ca$_V\alpha_1$), auxiliary α_2/δ (Ca$_V\alpha_2/\delta$), β (Ca$_V\beta$), and γ (Ca$_V\gamma$) subunits (2–8). The auxiliary subunits are believed to modulate channel properties and assist in trafficking of the channels to the plasma membrane (9, 10). A recent cryo-electron microscopy study of the 3D structure of the Ca$_V$1.1 voltage-gated calcium channel [Protein Data Bank (PDB) ID code: 5GJV] reveals that the interaction between pore and auxiliary subunits is driven by protein–protein interactions (11). Small molecules that disrupt these interactions could provide tools to study them in vivo and could potentially serve as lead compounds for the development of therapeutic agents to treat a range of neurological disorders associated with Ca$_V$s. Specifically, Ca$_V$2.2 is a clinically validated target for the treatment of human chronic pain (12–14), neuropathic pain (15), and epilepsy (16) and has been implicated in mechanisms of neuronal excitotoxicity (17).

Among the Ca$_V$ auxiliary subunits, Ca$_V\beta$ subunits increase the surface expression of Ca$_V$ channels and regulate their biophysical properties (18, 19). Ca$_V\beta$ subunits are encoded by four

different genes, Ca$_V\beta_{1-4}$, including multiple splice variants. Their 3D structure reveals the presence of Src homology 3 (SH3) and guanylate kinase (GK) domains connected by a HOOK region. One of these structures (PDB ID code: 1VYT) corresponds to the cocrystal structure of the β_3-subunit and the α-interacting domain (Ca$_V\alpha_{1-AID}$) of Ca$_V$ channels (20). It shows that Ca$_V\alpha_{1-AID}$ is a 25-residue α-helical structure that tightly binds to a well-defined groove on the GK domain of the β subunit (21–25). The structure reveals the presence of three subcavities that accommodate the side chains of Tyr-437, Trp-440, and Ile-441, respectively (22). These residues are considered hot spots, amino acids that are critical to the protein–protein interaction (26–30). Hot spots are amino acids that contribute at least 1.4 kcal·mol^{-1} to the Gibbs free energy of binding (28–32). Small molecules that mimic the position of hot spots on Ca$_V\alpha$ or that bind tightly to hot spots on Ca$_V\beta$ should disrupt the tight Ca$_V\alpha_1$·Ca$_V\beta$ protein–protein interaction. To date, no small-molecule antagonists of the Ca$_V\alpha_1$·Ca$_V\beta$ interaction have been identified.

Disruption of protein–protein interactions with small molecules is generally considered challenging (33) because of the

Significance

Voltage-gated ion channels, such as Ca$_V$2.2, consist of pore-forming and auxiliary subunits that interact through protein–protein interactions. We develop a small-molecule antagonist of the protein–protein interaction between the calcium channel alpha pore-forming domain (Ca$_V\alpha$) and beta subunits (Ca$_V\beta$). The compound suppresses trafficking of Ca$_V$2.2 channels to the cell membrane and inhibits Ca$_V$2.2 activity by acting intracellularly. This allows peripheral access and eliminates the need of intrathecal administration. Indeed, in vivo systemic administration of the small molecule reduces neuropathic pain behavior in animal models. Our compounds serve as chemical tools to explore the Ca$_V\alpha$·Ca$_V\beta$ interaction in vivo and as a starting point for the development of therapeutics for the treatment of a range of disorders associated with calcium channels.

typically large binding interfaces (>1,000 Å^2) that result in tightly bound stable complexes. However, there has been a gradual increase in the number of small-molecule antagonists of protein–protein interactions over the past decade (34–38). It has been suggested that these small molecules work by engaging or mimicking hot spots located at the protein–protein interface. Protein–protein interactions such as that of the Ca$_V$α$_1$·Ca$_V$β protein–protein interaction are classified as secondary interactions, given that the interface is composed primarily of an α-helix binding to a well-defined cavity. In the past, these interactions have been amenable to disruption with peptides or peptidomimetics (34, 39, 40). Several small molecules have been developed to successfully disrupt secondary interactions such as Bcl-xL·Bak (41), IL-2·IL-2Rα (42), and MDM2·p53 interactions (43).

To identify small molecules that inhibit the Ca$_V$α$_1$·Ca$_V$β protein–protein interaction, we resorted to structure-based computational screening of commercial libraries. Top candidates were purchased and tested for inhibition with fluorescence polarization (FP) using fluorescently labeled Ca$_V$α$_{1-AID}$. Starting with hit compound **1** (BTT-3), we prepared several derivatives, which eventually led to **6** (BTT-266), a small molecule that disrupted the binding of Ca$_V$α$_{1-AID}$ to the Ca$_V$β$_3$ subunit with single-digit micromolar inhibition constants. The binding mode of **6** revealed the presence of a salt-bridge interaction between the carboxylate moiety of the compound and the guanidium ion of Arg-307 on Ca$_V$β$_3$. To validate this binding mode, we synthesized compounds lacking a carboxylate and mutated Arg-307 to evaluate its role on the activity of compound **6**. We further validated the predicted binding mode of **6** through the synthesis of a series of derivatives. This led to **14** (BTT-369), a derivative with a cell-permeable tetrazole moiety instead of the carboxylic group of **6**. Patch-clamp experiments explored the effect of **6**, **14**, and an inactive analog **2** (BTT-245) on the function and trafficking of the Ca$_V$2.2 calcium channel. Finally, **6**, **14**, and the inactive analog **2** were evaluated in animal models of neuropathic pain.

Results

Structure-Based Virtual Screening.
The structural basis of the Ca$_V$α$_1$·Ca$_V$β interaction was revealed in a cocrystal structure between Ca$_V$β$_3$ and Ca$_V$α$_{1-AID}$ (Fig. 1*A*) (20). Ca$_V$α$_{1-AID}$ is a 25-residue α-helix that binds to a well-defined groove on the GK domain of Ca$_V$β$_3$ (Fig. 1*B*). Previous biophysical studies combined with site-directed mutagenesis on Ca$_V$α$_{1-AID}$ show the presence of three hot-spot residues (Tyr-437, Trp-440, and Ile-441) (22). The side chain of these residues is ensconced into three subsites. Small molecules that bind to the subsites and mimic Ca$_V$α$_{1-AID}$ hot spots are expected to disrupt this interaction. To identify small molecules that bind to Ca$_V$β at the protein–protein interaction interface, we resorted to virtual screening, focusing on the large binding cavity on Ca$_V$β$_3$. SiteMap (44) scoring of the cavity leads to a SiteScore of 1.01, suggesting that the pocket is highly druggable (45). Therefore, small molecules that bind to this pocket have the potential to exhibit in vivo efficacy similar to those of Food and Drug Administration-approved drugs. We stipulated that a small molecule that binds to this pocket will disrupt the Ca$_V$α$_1$·Ca$_V$β$_3$ protein–protein interaction. To that end, a total of 500,000 compounds from the ChemDiv commercial library were docked to the druggable pocket on Ca$_V$β$_3$ (Fig. 1*C*). The resulting protein-compound structures were scored and rank-ordered to select top candidates. The top 500 compounds from the GoldScore and ChemScore scoring functions were visualized, and 86 compounds were selected for purchase by visual inspection.

Screening Top Candidates.
To test for binding of the top-ranking compounds, we developed an FP assay. In general, the assay consists of a fluorescently labeled probe, typically a small peptide, and the target protein of interest. Upon binding to the larger protein, the labeled peptide experiences decreased motion, which leads to an increase in light polarization. Small molecules that displace the

peptide lead to a decrease in light polarization. The change in polarization can be used to quantify the extent of inhibition. Ca$_V$α$_1$·Ca$_V$β is ideally suited for an FP assay since the α-helix of Ca$_V$α$_{1-AID}$ is the minimum required epitope for binding to Ca$_V$β and the peptide is substantially smaller than Ca$_V$β. The Ca$_V$α$_{1-AID}$ peptide was synthesized and fluorescently labeled at its N terminus. The fluorescently labeled Ca$_V$α$_{1-AID}$ binds to Ca$_V$β$_3$ with a K_d of 21 ± 2 nM (Fig. 1*D*). This binding curve was used to select the protein concentration for titration with the compound. The FP assay was used to screen the 86 compounds that emerged from the computational screen at 50 μM. Four compounds inhibited binding of labeled peptide to Ca$_V$β$_3$ (*SI Appendix*, Fig. S1*A*). A follow-up concentration-dependent study showed that one compound, **1** (BTT-3), inhibited fluorescently labeled Ca$_V$α$_{1-AID}$ binding to Ca$_V$β$_3$ with a K_i of 6.7 ± 0.3 μM (*SI Appendix*, Fig. S1*B*) with a predicted binding mode shown in *SI Appendix*, Fig. S1*C*.

Design, Synthesis, and Binding Studies of Derivatives.
To further probe the predicted binding mode of **1** (*SI Appendix*, Fig. S1*C*) and to identify compounds with higher affinity, we designed and synthesized 14 derivatives (Fig. 2*A* and *SI Appendix*, Figs. S2–S8). The binding mode of **1** revealed that the R$_4$ group of the compound binds to a pocket on Ca$_V$β$_3$ occupied by Tyr-437 on Ca$_V$α$_1$. The R$_4$ pocket is a long, narrow binding site that can accommodate an additional substituent at the *para* position of the benzene ring. We introduced a piperazine ring at the *para* position of the benzene ring at R$_4$ in compound **3** (BTT-268) and a pyridine in compound **4** (BTT-267) at the same position. Although **3** did not bind, **4** inhibited the protein–protein interaction.

In addition to R$_4$, we made modifications at the R$_2$ moiety. The phenyl group of the R$_2$ substituent of **1** is solvent-exposed, and the group is engaged in favorable interactions with several hydrophobic residues that include Val-192, Met-195, Met-196, and Ala-199 (*SI Appendix*, Fig. S9). We modified this group to an isopropyl moiety in compound **5** (BTT-265), which led to complete loss of binding. This suggests that the R$_2$ aromatic group of **1** is essential for binding.

We stipulated that the rotatable bonds of the R$_1$ moiety may lead to unfavorable entropy of binding, especially considering that this group is likely fixed into the pocket occupied by Ile-441. We converted the butyric acid to a benzoic acid moiety in **6** (BTT-266), which resulted in a substantial increase in affinity to a K_i of 1.4 ± 0.1 μM. Unlike several of the compounds that did not completely inhibit the Ca$_V$α$_1$·Ca$_V$β$_3$ protein–protein interaction at high concentrations, likely due to poor solubility, **6** showed complete inhibition (Fig. 2*B*). Compound **6** possesses a chiral center at its core pyrazoline ring. Molecular docking of (*R*)-**6** and (*S*)-**6** resulted in two different binding modes for the enantiomers as expected (Fig. 2*C* and *SI Appendix*, Fig. S10). The (*S*)-**6** binding mode appears to be the most plausible, considering the excellent overlap between three of the compound substituents with three of the most critical hot spots on Ca$_V$α$_{1-AID}$, namely Tyr-437, Trp-440, and Ile-441 (Fig. 2*D* and *SI Appendix*, Fig. S11). The R$_3$ and R$_4$ substituents of (*S*)-**6** occupy the same position as Tyr-440 and Trp-437 of Ca$_V$α$_{1-AID}$, respectively. The R$_1$ substituent of (*S*)-**6** that bears the benzoic acid moiety occupies the same position as the side chain of Ile-441. Interestingly, just as in compound **1**, the carboxylate of **6** is involved in a salt-bridge interaction with Arg-307 (Fig. 2 *C* and *E*). Salt-bridge interactions are commonly found in small-molecule protein–protein interaction inhibitors. We have previously shown that disruption of the uPAR·uPA protein–protein interaction by IPR-803 was completely dependent on a salt bridge (46) that was later independently confirmed by crystallography (47). To confirm the importance of the salt bridge, we used the FP assay to test whether a methyl ester precursor of **6**, namely **7** (BTT-269) or **2** (BTT-245), a ketone derivative of **1**, binds to Ca$_V$β$_3$. Both **2** and **7** closely resemble **6**, but they do not possess the negative charge of the carboxylate moiety of **6**. Both **2** and **7** nearly completely
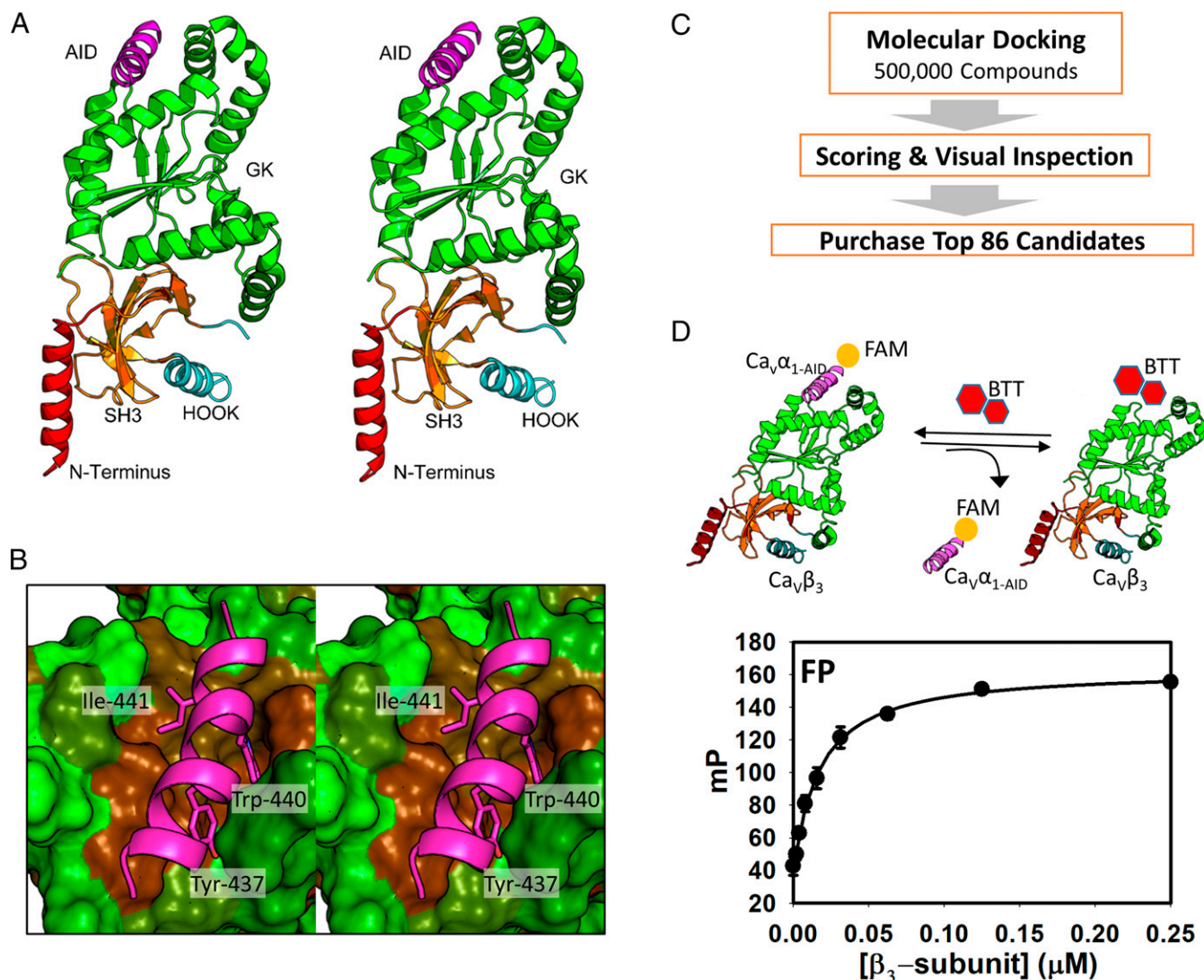
Fig. 1. Computational screening followed by biochemical testing identifies a compound that binds to Ca$_V$β$_3$. (A) 3D structure of Ca$_V$α$_1$·Ca$_V$β (PDB ID code: 1VYT). The AID, the GK domain, the SH3 domain, the HOOK domain that links GK and SH3, and the N terminus are shown in violet, green, orange, cyan, and red ribbon representation, respectively. (B) Stereo close-up view of the Ca$_V$α$_{1\text{-AID}}$ in complex Ca$_V$β$_3$ (PDB ID code: 1VYT). Ca$_V$α$_{1\text{-AID}}$ is depicted as a magenta ribbon, and hot spot residues are shown as capped sticks. Ca$_V$β$_3$ is shown in a solvent-accessible surface area color-coded by hydrophobicity ranging from less hydrophobic (green) to more hydrophobic (brown). (C) Schematic depicting the workflow that was used for the structure-based computational screening. (D, Upper) A depiction of the FP assay. (Lower) The plot corresponds to the change in FP as a result of titration of Ca$_V$β$_3$ with increasing concentration of fluorescently labeled Ca$_V$α$_{1\text{-AID}}$ peptide.

lost their ability to disrupt the Ca$_V$α$_1$·Ca$_V$β$_3$ interaction, confirming the importance of the salt bridge. These results lend further credence to the predicted binding mode of (S)-**6**. Carboxylic acids are known to reduce cell permeability. A common medicinal chemistry strategy to maintain the charge of the carboxylate while improving cell permeability is to replace the carboxylate with a tetrazole moiety. To that end, we prepared **14** (BTT-369). The compound possessed a K_i identical to that of **6**. Other changes to R$_1$ were made in compound **11** (BTT-274). The twofold reduction in binding affinity suggests that the amide bond is optimal at this position.

We modified additional substituents on **6** to further confirm its binding mode. The importance of a phenyl group at R$_2$ was established by the introduction of a benzyl moiety at R$_2$ in **9** (BTT-278), which led to compete loss of inhibition. Introduction of methoxy group at the *para* position of the benzene group of **6** in **10** (BTT-276) led to a twofold reduction in binding.

Finally, we modified the R$_3$ group of **6** by replacing the methyl group by a chlorine at the *para* position in **8** (BTT-280). This

resulted in little change to the binding affinity of the compound. A methoxy group in compound **12** (BTT-368), on the other hand, resulted in complex loss of binding. An imidazole phenyl moiety at R$_3$ in compound **15** (BTT-371) also resulted in complete loss of binding, consistent with the predicted binding mode of these compounds showing a constricted binding pocket at R$_3$.

It is worth noting that the inhibition curves for **6** and other compounds are steeper than usual, suggesting potential aggregation. To rule out the possibility that the inhibition of the Ca$_V$α$_1$·Ca$_V$β$_3$ interaction is due to aggregation, we repeated the concentration-dependent FP study of **6** using 0.05 and 0.25% Triton X-100 (*SI Appendix*, Fig. S12A). We find that even a 25-fold increase in detergent from 0.01 to 0.25% had no effect on the inhibition curves of **6**; the increase of Triton levels to 0.25% appears to have slightly improved the potency of the compound. Next, we used centrifugation to spin down the sample to eliminate all potential aggregates. As shown in *SI Appendix*, Fig. S12B, there was no difference in inhibition of the Ca$_V$α$_1$·Ca$_V$β$_3$ interaction by **6**
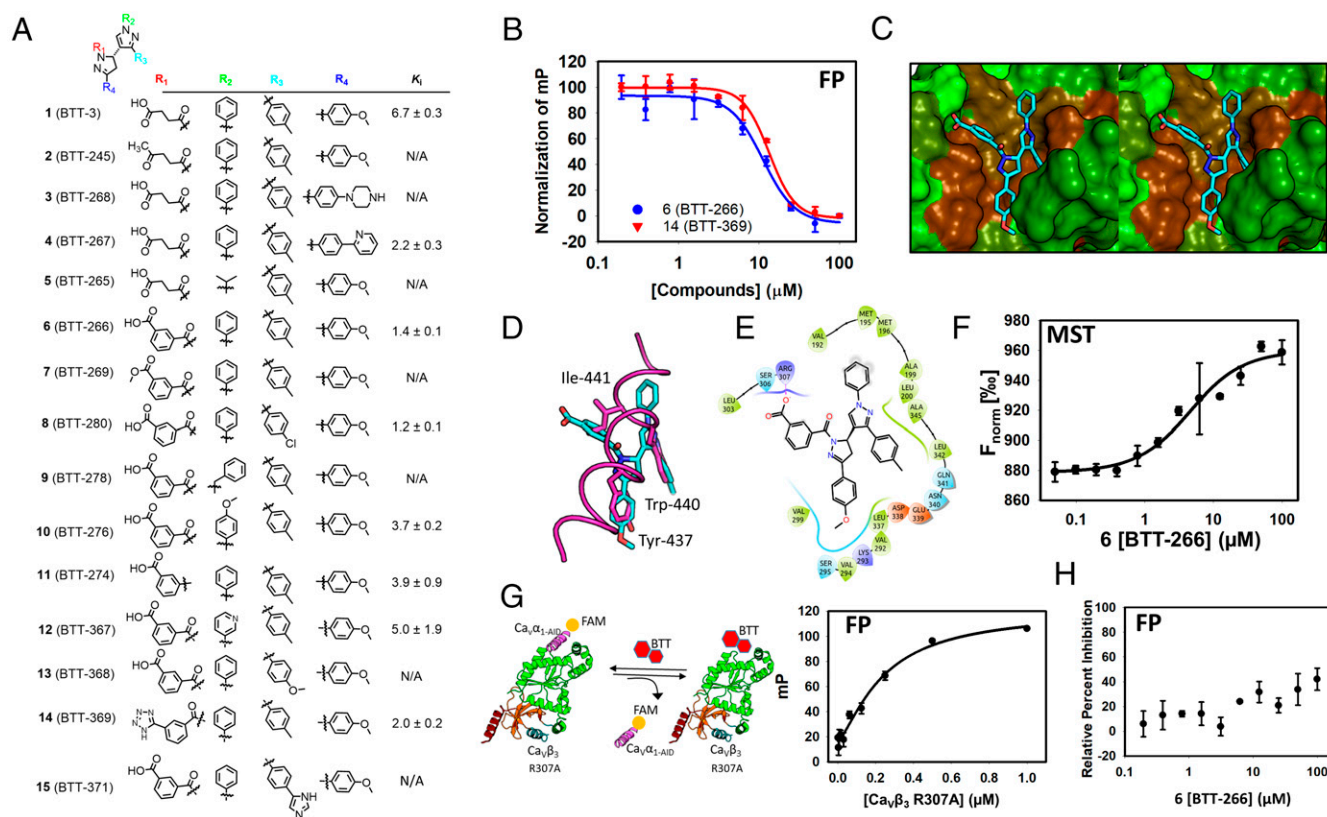
Fig. 2. Design and synthesis of a focused library identifies **6** (BTT-266) that inhibits the $Ca_V\alpha \cdot Ca_V\beta_3$ protein–protein interaction. (*A*) Chemical structure of derivatives that were designed and synthesized based on the structure of **1**. (*B*) The FP assay is used to determine an inhibition constant for **6**. (*C*) Binding mode of **6** to $Ca_V\beta_3$. This model was generated by molecular docking of the compound to the crystal structure of $Ca_V\beta_3$. The compound is shown as capped sticks and is color-coded by atom type (cyan, red, and blue correspond to carbon, oxygen, and nitrogen, respectively). $Ca_V\beta_3$ is shown in a solvent-accessible surface color-coded based on hydrophobicity (green, less hydrophobic; brown, more hydrophobic). (*D*) The binding mode of **6** superimposed on the binding mode of $Ca_V\alpha_{1-AID}$ (PDB ID code: 1VYT) shown in magenta tube rendering. Compound **6** is shown in capped-sticks representation color-coded by atom type. Hot spots on $Ca_V\alpha_{1-AID}$ are shown as magenta capped sticks to illustrate the overlap with substituents on **6**. (*E*) A 2D representation of the binding mode of **6** shown in *C* and *D*. The schematic shows the compound chemical structure along with the residues that are involved in intermolecular interactions with the compound. Hydrophobic, positively charged, negatively charged, and polar residues are colored green, blue, red, and cyan, respectively. Solvent-exposed atoms are shown by gray circles in the background. The salt bridge between Arg-307 and the compound is shown by a pink line. (*F*) The binding curve that emerged from the use of MST to establish direct binding of compound **6**. Curve-fitting analysis led to a K_d of 3.6 ± 1.1 µM. (*G*) An FP assay was developed using the $Ca_V\beta_3$ Arg-307-Ala (R307A) mutant titrated to the $Ca_V\alpha_{1-AID}$ fluorescently labeled peptide. The binding constant obtained from this analysis is 3.6 ± 1.1 µM. (*H*) Compound **6** does not inhibit the protein–protein interaction between $Ca_V\beta_3$ Arg-307-Ala as evidenced by a lack of displacement of fluorescently labeled $Ca_V\alpha_{1-AID}$ bound to the mutated $Ca_V\beta_3$.

in the presence or absence of spin down. Finally, we tested whether compound **6** inhibits unrelated tight protein–protein interactions, which would be expected if the compounds are inhibiting through aggregation. We used an FP assay that we developed for the tight single-digit nanomolar-affinity protein–protein interaction between the TEAD4 transcription factor and its coactivator Yap1. The compounds showed no inhibition of this interaction (*SI Appendix,* Fig. S12C). Collectively, these results suggest that inhibition of the $Ca_V\alpha_1 \cdot Ca_V\beta_3$ interaction by our compounds is not due to aggregation. Steep curves may be more common among compounds that target single-digit nanomolar-affinity interactions that occur over a large protein–protein interaction interface, as reported for ABT-737, a BCl-2 antagonist (48).

Direct Binding Confirmed by Label-Free Microscale Thermophoresis. To confirm direct binding of **6** to $Ca_V\beta_3$, we resorted to label-free microscale thermophoresis (MST) (Fig. 2*F*) (49). The method takes advantage of a laser-induced temperature gradient. The molecules migrate along the gradient, and their movement over time is monitored by a fluorescent microscope, resulting in characteristic traces as shown in *SI Appendix,* Fig. S13. To obtain a binding affinity, a concentration-dependent study is performed with a fixed

concentration of protein. If binding occurs, the thermophoretic signal will change with respect to concentration and is used to derive a dissociation constant, K_d. Unlabeled proteins have been successfully used to explore small-molecule binding with MST (50). The raw data shown in *SI Appendix,* Fig. S13 were used to generate a binding curve shown in Fig. 2*F*. The curves led to a K_d of 3.6 ± 1.1 µM. The MST binding constant is consistent with the K_i of 1.4 ± 0.1 µM that was obtained from the FP assay.

Site-Directed Mutagenesis Confirms a Critical Salt Bridge. The binding mode of **6** reveals that the compound forms a salt-bridge interaction with Arg-307 through a benzoic acid moiety. The removal of the charge from the compound, as in methyl ester **7**, led to complete loss of inhibition of the $Ca_V\alpha_1 \cdot Ca_V\beta_3$ interaction. To further confirm the importance of this salt bridge and to establish the predicted binding mode, we mutated Arg-307 to alanine. The resulting $Ca_V\beta_3$ Arg-307-Ala mutant binds to $Ca_V\alpha_{1-AID}$ with a K_d of 240 ± 59 nM (Fig. 2*G*). The reduction of K_d by nearly 10-fold suggests that Arg-307 is important for the $Ca_V\alpha_{1-AID} \cdot Ca_V\beta_3$ protein–protein interaction and could potentially be considered a hot spot. We used the $Ca_V\beta_3$ Arg-307-Ala mutant to develop an FP assay to test whether binding of the mutant protein to $Ca_V\alpha_{1-AID}$ is
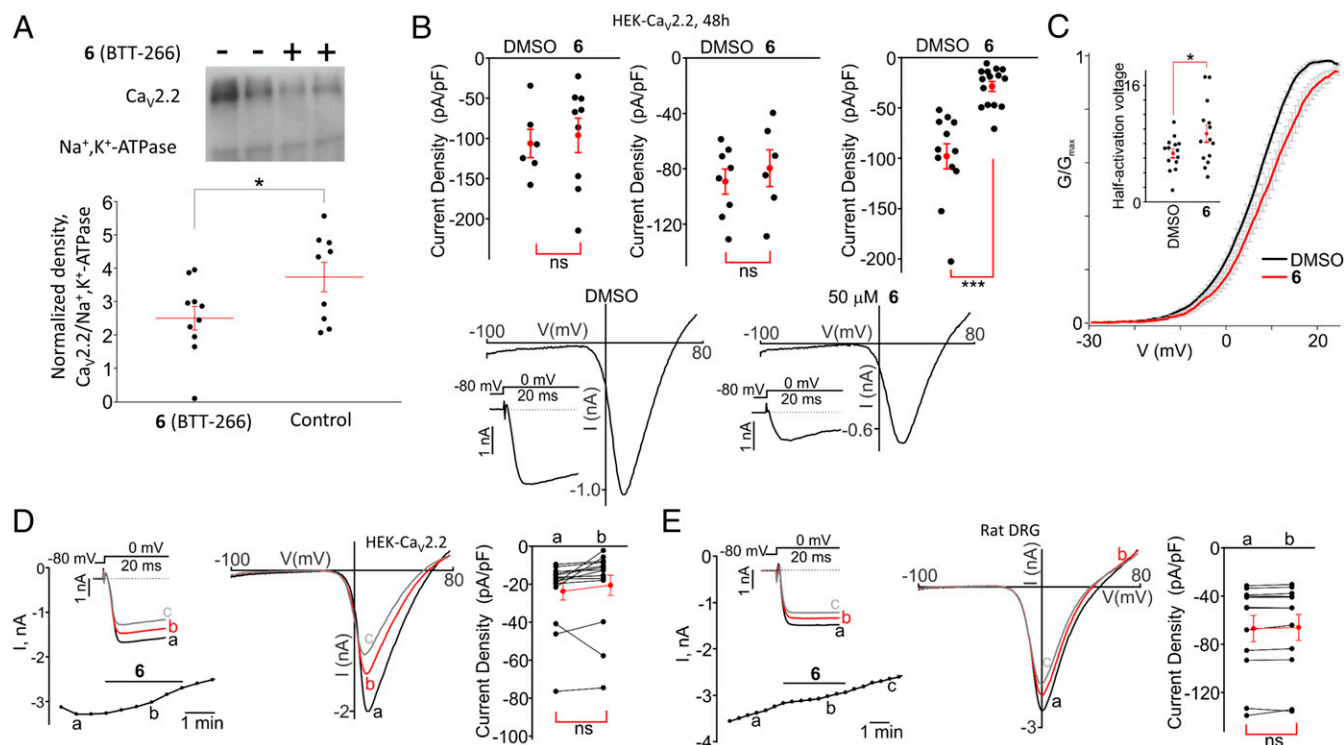
Fig. 3. Compound **6** decreases the cell-surface presentation of Ca$_V$2.2 channels. (*A*) Western blot analysis of cell-surface biotinylated proteins isolated from HEK-Ca$_V$2.2 cells treated with **6** (BTT-266) (+; *n* = 10) or with the vehicle control DMSO (−; *n* = 9) for 48 h. (*Upper*) A representative blot probed with the Ca$_V$2.2 antibody and the Na$^+$,K$^+$-ATPase antibody. (*Lower*) A comparison of the amounts of cell-surface biotinylated Ca$_V$2.2 proteins normalized to that of Na$^+$,K$^+$-ATPase. *P < 0.05. (*B*) (*Upper*) Summary data of the current densities recorded in HEK-Ca$_V$2.2 cells pretreated for 48 h with the vehicle (DMSO) or 10 μM **6** (*n* = 9) (*Left*), 25 μM **6** (*n* = 6) (*Center*), or 50 μM **6** (*n* = 15) (*Right*). *P < 0.001; ns, not significant. (*Lower*) Sample traces of the current–voltage relationships acquired during the voltage ramps from −100 mV to +80 mV in the DMSO (*Left*) and **6** at 50 μM (*Right*) groups. *Insets* show the Ca$_V$2.2 currents activated by depolarizing pulses to 0 mV. (*C*) Effect of **6** on the voltage dependence of activation of Ca$_V$2.2 channels in HEK-Ca$_V$2.2 cells pretreated with the vehicle or the indicated compounds for 48 h. The G–V curves are shown. The *Inset* shows a comparison of half-activation potentials in DMSO- and 50 μM **6**-pretreated HEK-Ca$_V$2.2 cells (48 h). (*D* and *E*, *Left*) Time courses of Ca$_V$2.2 currents recorded in an HEK-Ca$_V$2.2 cell (*D*; *n* = 15) or in a DRG neuron (*E*, [BaCl$_2$]$_{out}$ = 2 mM; *n* = 12) during acute applications of **6** (50 μM). *Insets* show the superimposed traces of Ca$_V$2.2 currents activated by depolarizing pulses to 0 mV in the absence and presence of **6**. (*Center*) The corresponding current–voltage relationships obtained in the absence and presence of **6**. (*Right*) Summaries of the data. Compound **6** was applied as indicated by the horizontal bars. a, b, and c show the times when the current traces were recorded. ns, not significant.

inhibited by compound **6** (Fig. 2*G*). Interestingly, compound **6** lost nearly all its affinity to the Ca$_V$β$_3$ Arg-307-Ala mutant, as shown in Fig. 2*H*. This loss of affinity was similarly observed in the other compounds (*SI Appendix*, Fig. S14). This further confirms the importance of the salt-bridge interaction and validates the binding mode of the compound to Ca$_V$β$_3$.

Compound 6 Reduces Trafficking of Ca$_V$2.2 to the Plasma Membrane. Previous studies have shown that Ca$_V$α$_1$·Ca$_V$β interaction is responsible for channel trafficking, and other studies have suggested that disruption of this interaction may affect the function of the calcium channel. Here, we use **6** to explore these questions. First, we determined whether **6** affects the targeting of the Ca$_V$2.2α$_1$ subunit to the plasma membrane. We employed a surface biotinylation approach (Fig. 3*A*). We found that at 50 μM, **6** significantly decreased surface presentation of the Ca$_V$2.2α$_1$ subunit. To confirm these results, we resorted to the patch-clamp technique. We recorded Ca$_V$2.2 currents in HEK-Ca$_V$2.2 cells pretreated with 10, 25, and 50 μM of **6** for 48 h (Fig. 3*B*). We found that the current densities obtained in the cells treated with 50 μM **6** were significantly decreased compared with group treated with vehicle (DMSO) (I$_{DMSO}$ = −98.0 ± 12.5 pA/pF, *n* = 12 vs. I$_6$ = −28.7 ± 5.0 pA/pF, *n* = 15; *P* < 0.001) (Fig. 3*B*). This is consistent with the surface biotinylation results.

We used **6** to explore whether compounds affected channel function. Notably, the conductance–voltage (G–V) curves for Ca$_V$2.2 were

shifted toward more positive potentials in HEK-Ca$_V$2.2 cells pretreated with **6** for 48 h (Fig. 3*C*). The mean half-activation potential was greater in the cells pretreated with **6** than in the control cells pretreated with DMSO for 48 h (DMSO: 6.7 ± 0.6 mV, *n* = 14; **6**: 9.4 ± 1.2 mV, *n* = 14, *P* < 0.05) (Fig. 3*C*, *Inset*). Conversely, acute application of 50 μM **6** did not affect Ca$_V$2.2 currents in either in HEK-Ca$_V$2.2 cells or rat dorsal root ganglion (DRG) neurons (Fig. 3 *D* and *E*), indicating that the compound does not inhibit the channel pore directly. The inactive analog **2**, which did not inhibit the Ca$_V$α$_1$·Ca$_V$β$_3$ protein–protein interaction, did not affect the Ca$_V$2.2 current amplitudes in HEK-Ca$_V$2.2 cells when it was used acutely or as a long-term treatment (Fig. 4*A*).

Compound 14 Modulates the Voltage Dependence of Activation and Steady-State Inactivation of Ca$_V$2.2. When activated by depolarizing pulses to 0 mV from a holding potential of −80 mV, the densities of Ca$_V$2.2 currents were significantly smaller in HEK-Ca$_V$2.2 cells pretreated for 48 h with 50 μM **14** than in cells treated with 50 μM **2** or DMSO (48 h; **14**: −11.1 ± 2.4 pA/pF, *n* = 12; **2**: −79.2 ± 8.2 pA/pF, *n* = 9; DMSO: −74.8 ± 7.0 pA/pF, *n* = 15; *P* < 0.001) (Fig. 4*A*). The apparent IC$_{50}$ for inhibition of Ca$_V$2.2 currents by **14** is 31 μM (Fig. 4*B*).

Since the Ca$_V$α$_1$·Ca$_V$β$_3$ protein–protein interaction may modulate the voltage dependence of activation and steady-state inactivation of Ca$_V$2.2α$_1$, and considering that the values of Ca$_V$α$_1$ half-activation and half-inactivation potentials were more
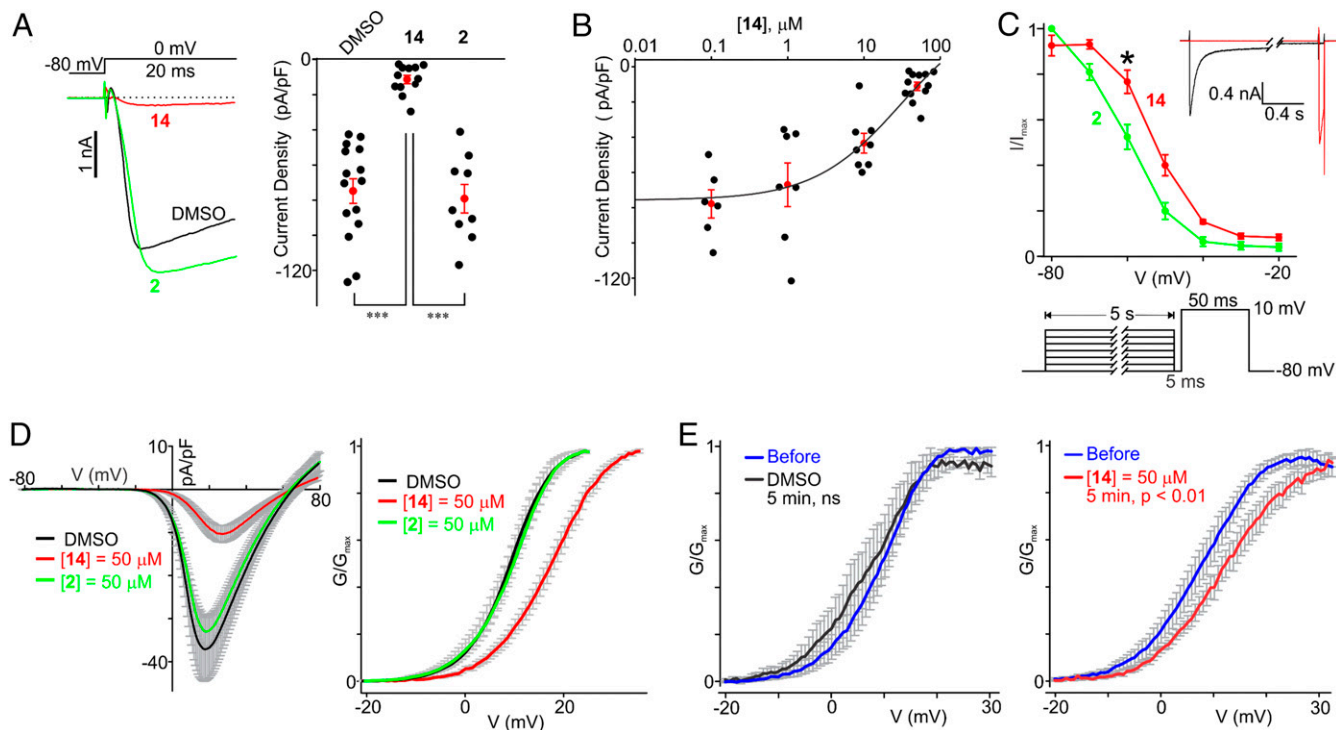
Fig. 4. Compound **14** (BTT-369) reduces the current density and modulates the voltage-dependence of activation and steady-state inactivation of Ca$_V$2.2. (*A*) The Ca$_V$2.2 current densities in HEK-Ca$_V$2.2 cells pretreated for 48 h with DMSO (*n* = 15), **14** (*n* = 12), or **2** (*n* = 9). (*Left*) the superimposed raw sample traces of Ca$_V$2.2 currents acquired during the 20-ms depolarizing pulses in HEK-Ca$_V$2.2 cells pretreated with the indicated compounds for 48 h. (*Right*) Summary of the data. ***P < 0.001. (*B*) The concentration–effect curve for **14**. HEK-Ca$_V$2.2 cells were pretreated with various concentrations of compound **14** for 48 h. Ca$_V$2.2 currents were acquired during 20-ms depolarizing pulses, and the current densities were calculated as a ratio of the peak current amplitude and each cell capacitance (0.1 μM, *n* = 6; 1 μM, *n* = 7; 10 μM, *n* = 8; 50 μM, *n* = 12). The line is the fit of the data to the four-parameter logistic function. The apparent IC$_{50}$ value is 31 μM. The same datasets for 50 μM **14** (BTT369) were used in *A* and *B*. (*C*) Effect of **2** (BTT-245) and **14** on the voltage dependence of the steady-state inactivation of Ca$_V$2.2 channels. The *Inset* shows two superimposed traces acquired during the steady-state inactivation protocol shown below the plot. HEK-Ca$_V$2.2 cells were pretreated with the indicated compounds for 48 h. *P < 0.05. (*D*) Effects of **2** and **14** on the voltage dependence of the activation of Ca$_V$2.2 channels in HEK-Ca$_V$2.2 cells pretreated with the vehicle or the indicated compounds for 48 h. (*Left*) The average current–voltage relationships acquired during voltage ramps for each test group. (*Right*) The average G–V curves for each treatment group. The gray vertical lines are error bars indicating SEM. (*E*) Acute effects of DMSO and **14** on the voltage dependence of the activation of Ca$_V$2.2 channels in HEK-Ca$_V$2.2 cells. (*Left*) Average G–V curves before and after 5-min incubation with DMSO (*P* > 0.05). (*Right*) Average G–V curves before and after 5-min incubation with **14** (*P* < 0.01). The gray vertical lines are error bars indicating SEM. ns, not significant.

negative in Ca$_V$α$_1$·Ca$_V$β$_3$-coexpressing cells (51, 52), we explored whether **14** can modulate the voltage dependence of steady-state inactivation and/or activation of Ca$_V$2.2 in HEK-Ca$_V$2.2 cells. Fig. 4*C* shows that the Ca$_V$2.2 steady-state inactivation curves were significantly shifted toward more positive potentials in HEK-Ca$_V$2.2 cells pretreated for 48 h with **14** (50 μM, V$_{0.5,\ inact}$ = −52.9 ± 1.3 mV, *P* < 0.05, *n* = 10) than in the control group (**2**; 50 μM, V$_{0.5,\ inact}$ = −61.6 ± 2.0 mV, *n* = 10). While analyzing current–voltage relationships obtained during voltage ramps (Fig. 4*D*), we also found that the mean half-activation potential for Ca$_V$2.2 channels exhibited a more positive value in HEK-Ca$_V$2.2 cells pretreated for 48 h with **14** (50 μM, V$_{0.5,\ act}$ = 16.5 ± 1.1 mV, *P* < 0.001, *n* = 12) than in the controls (DMSO: V$_{0.5,\ act}$ = 8.7 ± 1.1 mV, *n* = 12; **2**: 50 μM, V$_{0.5,\ act}$ = 8.5 ± 1.4 mV, *n* = 9). These two findings are consistent with the hypothesis that **14** disrupts Ca$_V$α$_1$·Ca$_V$β$_3$ interactions.

Thus far, we used only long-term pretreatments (48 h) of HEK-Ca$_V$2.2 cells with **6** and **14**. Since **14** lacks the negatively charged carboxylate group in the R$_1$ substituent of **6**, which is replaced with an isosteric tetrazole moiety, **14** is more membrane permeable than **6**. The data presented above suggested that **14** may disrupt the intracellular Ca$_V$α$_1$·Ca$_V$β$_3$ protein–protein interaction in live cells. Therefore, we then asked whether acute short-term treatments with **14** in patch-clamped HEK-Ca$_V$2.2 cells could modulate the half-activation potential for Ca$_V$2.2 channels. No

significant change in the mean half-activation voltage value was observed in patch-clamped HEK-Ca$_V$2.2 cells acutely treated with DMSO (before treatment: V$_{0.5,\ act}$ = 9.1 ± 1.6 mV; 5 min under DMSO: V$_{0.5,\ act}$ = 6.8 ± 3.3 mV, *n* = 3, *P* > 0.05) (Fig. 4*E*, *Left*). Conversely, a 5-min incubation with 50 μM **14** was sufficient to significantly shift the G–V curves of Ca$_V$2.2 toward more positive potentials (before treatment: V$_{0.5,\ act}$ = 6.4 ± 1.9 mV; 5 min under **14**: V$_{0.5,\ act}$ = 11.4 ± 1.7 mV, *n* = 7, *P* < 0.01) (Fig. 4*E*, *Right*), indicating that the Ca$_V$2.2 channel requires stronger depolarization to be activated in the presence of **14**.

Pharmacokinetic Properties of Compound 14. Voltage-dependence of activation and steady-state inactivation experiments in HEK-Ca$_V$2.2 revealed that compound **14** appears to be more potent than **6** or **2**. These observations suggest that **14** may be more efficacious in vivo than **6** and **2**. Before testing **14** in nociceptive and neuropathic pain using in vivo assays, we sought to understand the pharmacokinetic properties of the compound in the mouse. For i.v. administration, **14** was formulated as a solution at a final dose of 1 mg/kg. Plasma concentrations at various time points were determined using the LC-MS/MS technique (*SI Appendix*, Fig. S15). The elimination half-life of **14** was 0.29 h. The amount of time that the maximum concentration of the drug was present in plasma (Tmax) was 0.083 h, and the peak plasma concentration (Cmax) that

the drug achieved was 181.36 ng/mL. The area under the curve (AUC_{0-t}) concentration was 57.99 ng·mL^{-1}·h^{-1}.

For oral gavage administration, **14** was formulated as a solution at a final dose of 10 mg/kg. Plasma concentrations at various time points were again determined using the LC-MS/MS technique (*SI Appendix*, Fig. S15). The elimination half-life of **14** was 1.99 h. The Tmax in plasma was 1 h, and the Cmax was 164.7 ng/mL. The AUC 0-t concentration was 635.555 ng·mL^{-1}·h^{-1}. Taken together, these observations indicate that **14** has a significant lifetime in vivo and may exhibit notable therapeutic potential. Thus, there is a structure–activity relationship, **14** > **6** > **2**, in the chemical series, which points to potential druggability of the series and the potential to identify an optimal lead compound as well as the pharmacological validation and therapeutic potential.

Effects of Compound 6 on Acute Thermal Nociception in the Rat. A model of behavioral sensitivity using thermal stimulus was used to determine the acute analgesic properties of the candidate small molecules. Thermal stimulation serves to activate high-threshold primary afferent sensory fibers in the hind paw glabrous skin. These axons carry action potential discharges to the dorsal horn of the spinal cord to activate secondary nociceptive neurons which contribute to a behavioral response of paw withdrawal from the aversive stimulus. Systemic administration of **6** failed to elicit changes in the response latency at 1 or 10 mg/kg (Fig. 5*A*).

Neuropathic Pain Is Attenuated by Treatment with Compounds 6 and 14 but Not Compound 2. We next examined the effects of morphine and compounds **2** and **6** on established chronic nociceptive behavior in a model of neuropathic pain, tibial nerve injury (TNI), 28 d after surgery (Fig. 5*B*) (53). TNI induces prolonged chronic behavioral hypersensitivity to mechanical stimuli which lasts for several months and is generally insensitive to opioids such as morphine (53, 54). Before exposure to the compound, all injured animals exhibited pronounced mechanical allodynia (33.1 ± 5.9 mN; n = 8–10) in response to von Frey hair stimulation of the injured hind paw, compared with presurgery levels, which averaged 68.7 ± 3.7 mN (n = 8–10) (Fig. 5*C*). Pronounced attenuation of tactile hypersensitivity was observed at 1 h but not at 4 h after systemic administration of **6** (10 mg/kg, i.p.; 62.2 ± 3.1 mN; n = 16). The **6** dosing levels of 1 mg/kg and 0.1 mg/kg failed to alter behavior at 1 or 4 h. In contrast, systemic administration of morphine (5 mg/kg) and **2** (10 mg/kg, i.p.) was ineffective in reducing hypersensitivity, with levels averaging 32 ± 2.6 mN (n = 8) (Fig. 5*C*). That the paw-withdrawal threshold (PWT) returned to baseline by 4 h in **6**-injected rats is consistent with the turnover of drug over this period and is a limitation of this drug candidate. PWTs were increased significantly at both 1 and 24 h postinjection in rats exposed to **14** (0.1 mg/kg) 28 d after TNI compared with rats injected with **6** or vehicle control (Fig. 5*D*).

Discussion

The neuronal Ca$_V$2.2 voltage-gated Ca^{2+} channel is implicated in mediating neurotransmitter release in nociceptive neurons. Ca$_V$2.2 channels are large (>400 kDa) heteromeric assemblies composed of pore-forming α subunits and auxiliary α$_2$/δ and β subunits (2–8). The auxiliary subunits are believed to modulate the properties and assist in trafficking of the channels to the plasma
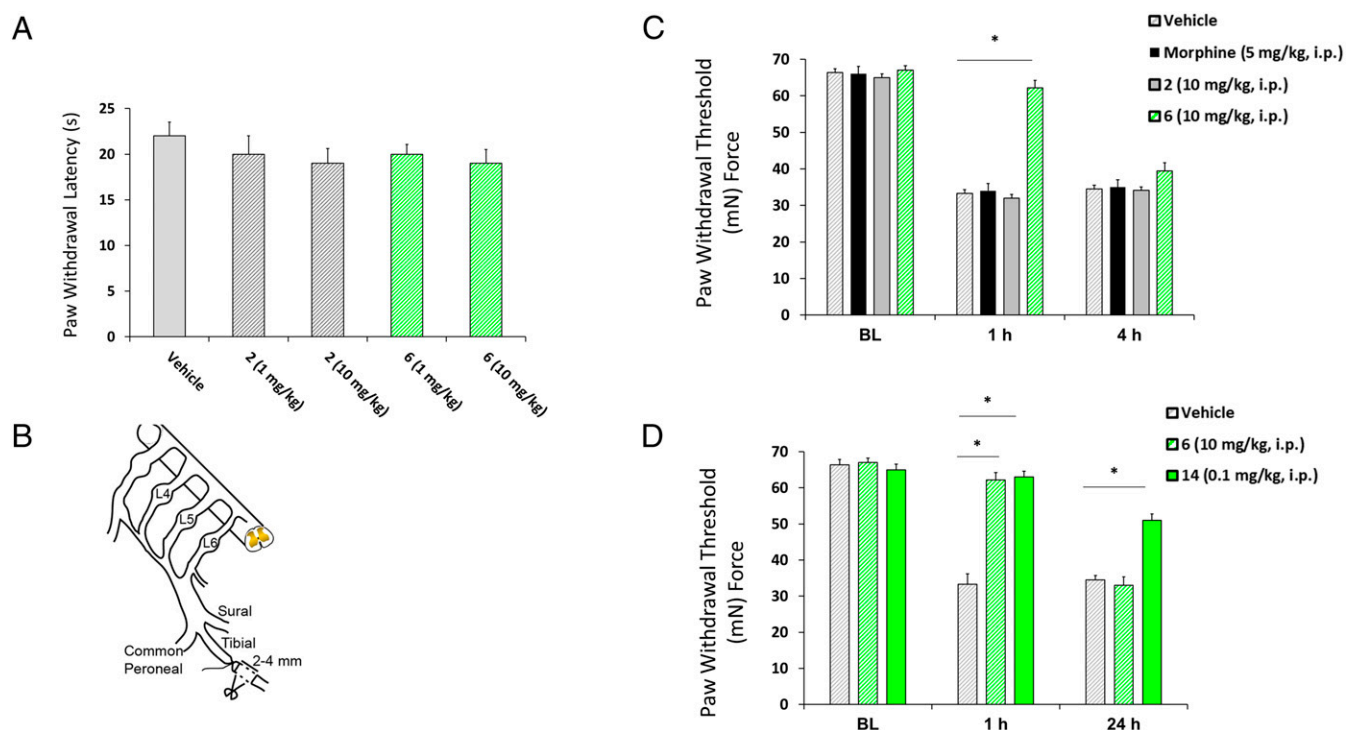

Fig. 5. Compounds **6** and **14**, but not **2**, reverse mechanical hypersensitivity in the TNI model of neuropathic pain. (*A*) Bar graph of paw withdrawal latency (in seconds) of rats (n = 6 per group) demonstrating a lack of analgesic effect for **2** or **6**. (*B*) Diagram of the sural, tibial, and common peroneal terminal nerve branches of the sciatic nerve and their dorsal root origins. Neuropathic pain was induced by ligation of the tibial nerve, and 2–4 mm of the nerve distal to the ligation was removed. (*C*) PWT (in milli-Newtons, mN) in response to von Frey stimulation to the paw ipsilateral to injury following a single i.p. administration of vehicle, morphine (5 mg/kg), **2**, or **6** (10 mg/kg, n = 8) at 4 wk after TNI. The ability of **6** (green striped bar) to reverse TNI-induced mechanical hypersensitivity was significantly different from that of **2** (solid gray bar) and morphine (black striped bar). *P < 0.05 versus **2** and morphine treatment in TNI rodents (mean ± SE; n = 8, repeated measures ANOVA with Tukey's post hoc test). BL, baseline. (*D*) At 4 wk, a single bolus injection of **14** (0.1 mg/kg) significantly reversed mechanical hypersensitivity at both 1 and 24 h post dosing. For comparison, reversal of mechanical hypersensitivity by **6** (10 mg/kg) was limited to 1 h. Data are shown as mean ± SE; n = 8; *P < 0.05 versus **6** and vehicle-treated TNI rodents; repeated-measures ANOVA with Tukey's post hoc test.

membrane (9, 10). The transmembrane α_2/δ subunit has recently received renewed interest for being the target of the anticonvulsant drugs gabapentin (Neurontin) and pregabalin (Lyrica), two moderately effective treatments for clinical neuropathic pain (15, 55). There is clear evidence showing dysregulation of Ca^{2+} homeostasis in many neurological diseases, and studies have demonstrated that Ca^{2+} channels are a clinically validated target for the treatment of human chronic pain (12–14) and neuropathic pain (15) and have been implicated in mechanisms of neuronal excitotoxicity (17). Most existing drug-discovery efforts targeting calcium channels have concentrated on the α pore-forming subunits. Protein–protein interactions between the pore-forming and auxiliary subunits, particularly the $Ca_V\alpha \cdot Ca_V\beta$ interaction, have been largely ignored.

Here, we report the discovery of a small molecule that modulates the $Ca_V\alpha_1 \cdot Ca_V\beta_3$ protein–protein interaction of Ca_Vs. We followed a simple approach that consisted first of docking more than 500,000 commercially available compounds to the large pocket at the $Ca_V\alpha \cdot Ca_V\beta_3$ interface. We visually inspected the top 500 candidates. Testing of 86 compounds led to **6**, which inhibited the $Ca_V\alpha_1 \cdot Ca_V\beta_3$ interaction with a K_i of 1.4 ± 0.1 μM. Using label-free MST, we confirmed that the compound binds directly to $Ca_V\beta_3$ and obtained a K_d that was nearly identical to the K_i from the FP assay. Interestingly, the binding mode of **6** reveals the presence of a salt-bridge interaction between its benzoic acid moiety and Arg-307. To confirm the presence of a salt bridge, we tested a methyl ester derivative of **6**, namely **7**, as well as a ketone derivative of **1**, namely **2**, both of which lacked a charged carboxylate. These compounds showed a complete loss of inhibition. To further establish the critical nature of the salt bridge, we mutated Arg-307 to alanine. We found that **6** completely lost its ability to inhibit the $Ca_V\alpha_1 \cdot Ca_V\beta_3$ interaction in the absence of Arg-307, further confirming the existence of the critical salt-bridge interaction. The importance of this salt bridge was further confirmed by the synthesis of **14**, a derivative of **6** that possesses a tetrazole moiety instead of carboxylic acid. The compound exhibited inhibition potency similar to that of **6**.

We explored whether the compounds affected calcium-channel trafficking and function. Previous studies have shown that the interaction with $Ca_V\beta$ is critical for $Ca_V2.2\alpha_1$ subunit trafficking to the plasma membrane. We demonstrated that pretreatment of HEK-$Ca_V2.2$ cells with **6** decreased the cell-surface presentation of $Ca_V2.2\alpha_1$ proteins. Using patch-clamp studies, we also found that the compound significantly attenuated channel density at the cell membrane. Longer treatment time was necessary due to the slow kinetics of internalization and degradation of $Ca_V2.2$ channels containing the $\alpha_2\delta$ subunit (56). Collectively, these results confirm previous studies that the $Ca_V\alpha_1 \cdot Ca_V\beta$ interaction is responsible for channel trafficking. Subsequently, we explored whether the compounds affected cation currents through the channel during an acute application to exclude a direct effect on the $Ca_V2.2\alpha_1$ subunit. Patch-clamp analyses revealed that **6** had no acute effect on the amplitude of Ba^{2+} currents through the channel. This is reasonable, considering the latest cryo-electron microscopy structure of $Ca_V1.1$ (PDB ID code: 5GJV). Using this structure, we constructed a homology model of $Ca_V2.2$ (*SI Appendix*, Fig. S16). The model, which closely resembles that of $Ca_V1.1$, shows that the $Ca_V\alpha_1 \cdot Ca_V\beta$ interaction is located outside the channel pore. Hence, disruption of the $Ca_V\alpha_1 \cdot Ca_V\beta$ interaction may not affect cation flow through the channel.

We also demonstrated that **6** and **14** may modulate the voltage dependence of $Ca_V2.2$ activation. It is well established that the interaction of $Ca_V\beta3$ and $Ca_V\alpha_1$ results in a shift of the half-maximum voltage of activation for $Ca_V2.2$ to more negative potentials (51, 52). A more negative half-activation potential for $Ca_V2.2$ means that the channel can be activated at more moderate membrane-depolarizing voltages. Conversely, disruption of the $Ca_V\alpha_1 \cdot Ca_V\beta$ protein–protein interaction is expected to shift the half-activation potential for $Ca_V2.2$ toward a more positive voltage, making it harder for the $Ca_V2.2$ channel to be activated

at the moderate depolarizing voltages. Consistently, we found that **14**, a membrane-permeable disruptor of the $Ca_V\alpha_1 \cdot Ca_V\beta$ protein–protein interaction, significantly shifted the G–V curves of $Ca_V2.2$ toward the positive potentials. The rightward shift of the mean half-activation potential was most pronounced after a 48-h pretreatment with **14**. However, even following a brief 5-min treatment in patch-clamped HEK-$Ca_V2.2$ cells, the compound was capable of significantly shifting the G–V curves for $Ca_V2.2$ toward more positive potentials (although in a lesser degree than observed after 48-h pretreatments). Thus, these data indicate that stronger depolarizations are needed to activate $Ca_V2.2$ in the presence of **14**.

N-type voltage-gated calcium channels ($Ca_V2.2$), largely localized to primary afferent terminals in laminae 1 and 2 of the dorsal horn, play an important role in pain signaling by contributing to the release of neurotransmitters such as glutamate, substance P, and calcitonin gene-related peptide (CGRP). Development of a highly efficacious, nonaddicting analgesic with a good side-effects profile has been challenging. Clinically approved blockers of this ion channel to date are encumbered by numerous off-target effects and exhibit narrow therapeutic windows. Novel small-molecule compounds that are nonaddictive and alter pain behavior following injury are sought for treatment of both subacute and chronic pain conditions. We tested whether **6** had an effect on rodent behavior in a neuropathic pain model. We found that **6** given systemically reversed TNI-hypersensitivity for 1 h but not 4 h, while the same dose of **2**, which did not inhibit the in vitro $Ca_V\alpha_1 \cdot Ca_V\beta$ interaction, had no effect. Similar behavioral effects were observed for **14** for up to 24 h, which is suggestive of sustained pain relief. These observed effects may be due in part to a possible pharmacologic block of presynaptic neurotransmitter release of neuropeptides or changes in the excitability of nociceptive neurons present in animals with chronic pain conditions. Moreover, this effect may be attributed to a state-dependent affinity and enhanced high-frequency activation patterns in pain syndromes. That **6** was unable to alter the behavioral responses to acute thermal nociception may be attributed to lower-frequency firing patterns associated with normal nociception (57).

In sum, we identified small molecules that inhibit the protein–protein interaction between pore and auxiliary subunits of a voltage-gated ion channel. The compounds are α-helical mimetics. It is likely that another, similar protein–protein interaction exists in other ion channels that can be targeted with small molecules. The profound in vivo efficacy of **14** at a dose of 0.1 mg/kg suggests that this compound offers the potential to develop new treatments for various neurological conditions associated with aberrant trafficking and function of calcium channels.

Materials and Methods

Virtual Screening. The crystal structure for $Ca_V\beta_3$ was obtained from the Research Collaboratory for Structural Bioinformatics (RCSB) Protein Databank (PDB ID code: 1VYT) (58). Structures were imported into SYBYL 8.0, a molecular modeling suite from Tripos, Inc., for predocking preparation. All binding partners, ions, and water molecules were removed. Hydrogen atoms were added, and the protonation states on polar residues were optimized with Reduce (version 3.03) (59). Structures were then loaded into Auto-DockTools (60) for further processing. Further details about the docking and scoring of compounds are provided in *SI Appendix*.

Protein Expression and Purification. The plasmid of the pET28a-$Ca_V2.2\beta_3$ subunit was transformed into a competent *Escherichia coli* BL21(DE3) strain. The culture was grown in LB medium at 37 °C to an OD_{600} of ∼0.6 and then was induced with 0.5 mM isopropyl β-d-1-thiogalactopyranoside at 16 °C for 16 h. Cells were collected by centrifugation and lysed by microfluidizer in lysis buffer (phosphate buffer, pH 7.6, 2 mM DTT). The His-$Ca_V\beta_3$ protein was purified at 4 °C using Ni-IMAC chromatography (His-Trap HP; GE Healthcare) and was eluted with 500 mM imidazole in lysis buffer with a gradient method. After the fractions consisting of His-$Ca_V\beta_3$ were combined and concentrated, the protein was further purified using size-exclusion chromatography (Superdex 200 prep grade; GE Healthcare) in PBS with 2 mM DTT.

FP and MST Analysis. FP was used in a competition format to test compounds for inhibition of the Ca$_V$α·Ca$_V$β$_3$ protein–protein interaction. A fluorescently labeled peptide that contains the region of Ca$_V$α that binds to Ca$_V$β$_3$ was synthesized. The fluorescent fluorescein-AID peptide was found to bind to Ca$_V$β$_3$ with a K_d of 21 ± 2 nM. The high affinity of the Ca$_V$β$_3$ probe suggests that introduction of the fluorescent label to the peptide had no impact on its binding affinity, which is close to the value that Minor and coworkers (22) measured using isothermal titration calorimetry. MST analysis was carried out to confirm direct binding of small molecules to Ca$_V$β$_3$. Further details about the experimental setup are provided in *SI Appendix*.

HEK-Ca$_V$2.2 Cell Culture. HEK293 cells stably expressing rat N-type Ca$_V$2.2α$_1$B, rat Ca$_V$β$_3$, and rat α$_2$δ-1 were obtained from Diane Lipscombe (Brown University, Providence, RI) (61). Cells were grown in DMEM supplemented with 10% FBS, 50 U penicillin, 50 μg/mL streptomycin, 5 μg/mL blasticidin, 5 μg/mL hygromycin, and 25 μg/mL zeocin at 37 °C in a humidified atmosphere of 95% air and 5% CO_2. For patch-clamp experiments, HEK-Ca$_V$2.2 cells were plated on glass coverslips and were cultured for 24–48 h.

DRG Neuron Isolation. All animal procedures were performed in accordance with NIH guidelines and were approved by the Indiana University School of Medicine Institutional Animal Care and Use Committee. Young adult Sprague–Dawley rats were anesthetized (3% isoflurane) and then decapitated. The spinal column was removed and cut open, and DRGs were harvested from the lumbar L4–L6 vertebral levels. The ganglia were incubated in DMEM containing collagenase (1 mg/mL; Worthington; LS04194) and protease (1 mg/mL; Worthington; LS02104) for 30–60 min, and DRG neurons were dissociated by triturating in DMEM supplemented with 10% FBS. The isolated DRG neurons were plated on glass coverslips coated with Growth Factor Reduced Matrigel (Thermo Fisher Scientific) and were cultured in Eagle's minimum essential medium (Invitrogen) supplemented with 0.2% BSA and 20 ng/mL NGF-2.5S (BD Biosciences) overnight at 37 °C in a water-jacketed 5% CO_2 incubator for the patch-clamp experiments.

Cell-Surface Protein Biotinylation and Western Blotting. Cell-surface protein biotinylation and Western blotting were performed as previously described (62). Briefly, HEK-Ca$_V$2.2 cells were treated with **6** (BTT-266) or the vehicle (DMSO) for 48 h. The surface proteins were biotinylated with 5 mM biotin-X-NHS (EMD Millipore) in PBS for 30 min at 4 °C. After biotinylation, cells were quenched and washed with PBS containing 100 mM glycine. Then, cells were lysed in ice-cold RIPA buffer containing the Halt protease inhibitor mixture (Thermo Fisher Scientific). The lysate was cleared by centrifugation, the preabsorbed avidin-agarose beads were added, and the resulting suspension was rotated for 30 min at 4 °C. The avidin-agarose beads were spun down and then washed three times with the complete lysis buffer. Proteins were eluted from the beads by incubation with SDS gel loading buffer supplemented with 1 mM DTT for 10 min at 70 °C. The eluted proteins were separated using 10% SDS-PAGE, transferred onto PVDF (Immun-Blot; Bio-Rad), and probed with the anti-Ca$_V$2.2-α$_1$B antibody from Alomone Labs (1:1,000 dilution; catalog no. AC002) and the Na$^+$,K$^+$-ATPase antibody (1:1,000 dilution; catalog no. 3010; Cell Signaling).

Whole-Cell Patch-Clamp Recordings in HEK-Ca$_V$2.2 Cells and DRG Neurons. The whole-cell patch-clamp technique was used to record Ca$_V$2.2 currents in HEK-Ca$_V$2.2 cells and rat DRG neurons as described elsewhere (63). Details of the experimental procedures used to carry out the patch-clamp recordings reported in this work are provided in *SI Appendix*.

Animals. Pathogen-free, adult, female Sprague–Dawley rats (weight at testing 150–200 g) (Harlan–Sprague–Dawley) were housed in a climate-controlled room on a 12-h light/dark cycle and were allowed to have food and water ad libitum. All procedures were approved by the Indiana University Animal Care and Use Committee and conformed to the *Guide for the Care and Use of Laboratory Animals* (64) for the use of laboratory animals. All behavioral experiments were conducted by experimenters blinded to the treatment conditions and small-molecule candidate identity. The experiments were replicated a minimum of two times with independent cohorts of animals.

Drug Delivery. For in vivo studies, small-molecule candidates **2**, **6**, and **14** were freshly prepared using saline (0.9%) on the day of the experiment. Morphine sulfate salt (Sigma-Aldrich) was freshly prepared on the day of the experiment in saline. All drugs were dissolved in 1 mL solution and administered by i.p. injection 1 h before all behavioral assays.

TNI. TNI was performed to model nerve injury-induced neuropathic pain as described previously (53, 65). Using isoflurane anesthesia (4% induction and 2% maintenance), we isolated the right sciatic nerve under aseptic surgical conditions by blunt dissection of the femoral biceps muscle, and the tibial nerve was tightly ligated with 5–0 silk and transected distal to the ligation. An additional 2–3 mm of the distal nerve stump was removed to prevent reinnervation by the proximal nerve. The overlying muscle and skin was then sutured in two separate layers. Sham-injured animals were subjected to all preceding procedures with the exception of ligation and transection. All animals were returned to the housing facility and allowed to survive for 28 d.

Assessment of Tactile Hypersensitivity. Mechanical stimuli were applied with seven filaments, each differing in the bending force delivered (10, 20, 40, 60, 80, 100, and 120 mN) and fitted with a flat tip and fixed diameter of 0.2 mm. The filaments were tested in the order of ascending force, with each filament delivered for 1 s. The withdrawal threshold stimulus was sequentially based on ascending force. A Hill equation was fitted to the function based on the percentage of specific responses to six stimulations to elicit a 50% withdrawal rate.

Foot Withdrawal to Thermal Stimulus. To evaluate the PWT to thermal stimulation, we used the Hargreaves' plantar test apparatus (Ugo Basile) (66). Measurements of the withdrawal latency of the paw began after the rats were habituated to the testing environment (infrared setting = 70). The measurements were repeated four times at 5-min intervals; the initial pair of measurements was not used. The averages of the three remaining pairs of measurements were employed as data.

Synthesis. The synthesis route that was used to prepare compounds in this work and the structural characterization of the compounds are provided in *SI Appendix*.

Statistical Analysis. Differences between means were compared by Student t tests. The biotinylation data were analyzed using an unpaired Student t test. The electrophysiological data were analyzed using an unpaired Student t test (Figs. 3 *B* and *C* and 4*B*) or a paired Student t test (Figs. 3*D* and 4*A*). Behavioral threshold values were statistically analyzed, and the significance of differences between the average of at least two preinjection tests and the mean obtained for each postinjection test was analyzed. In all tests, baseline data were obtained for the TNI-injured groups before drug or vehicle administration and were compared with the baseline values by repeated-measures ANOVA followed by the post hoc Tukey's multiple-comparison test. A P value less than 0.05 was considered to indicate statistical significance between treatment and nontreatment groups.

1. Atlas D (2013) The voltage-gated calcium channel functions as the molecular switch of synaptic transmission. *Annu Rev Biochem* 82:607–635.
2. Catterall WA (2000) Structure and regulation of voltage-gated Ca2+ channels. *Annu Rev Cell Dev Biol* 16:521–555.
3. Catterall WA (1993) Structure and modulation of Na+ and Ca2+ channels. *Ann N Y Acad Sci* 707:1–19.
4. Catterall WA (1996) Molecular properties of sodium and calcium channels. *J Bioenerg Biomembr* 28:219–230.
5. Catterall WA (1998) Structure and function of neuronal Ca2+ channels and their role in neurotransmitter release. *Cell Calcium* 24:307–323.
6. Hofmann F, Biel M, Flockerzi V (1994) Molecular basis for Ca2+ channel diversity. *Annu Rev Neurosci* 17:399–418.
7. Hofmann F, Lacinová L, Klugbauer N (1999) Voltage-dependent calcium channels: From structure to function. *Rev Physiol Biochem Pharmacol* 139:33–87.
8. Dolphin AC (2006) A short history of voltage-gated calcium channels. *Br J Pharmacol* 147:S56–S62.

9. Arikkath J, Campbell KP (2003) Auxiliary subunits: Essential components of the voltage-gated calcium channel complex. *Curr Opin Neurobiol* 13:298–307.
10. Yasuda T, et al. (2004) Auxiliary subunit regulation of high-voltage activated calcium channels expressed in mammalian cells. *Eur J Neurosci* 20:1–13.
11. Wu J, et al. (2016) Structure of the voltage-gated calcium channel Ca(v)1.1 at 3.6 Å resolution. *Nature* 537:191–196.
12. Altier C, et al. (2007) Differential role of N-type calcium channel splice isoforms in pain. *J Neurosci* 27:6363–6373.
13. Bourinet E, Zamponi GW (2005) Voltage gated calcium channels as targets for analgesics. *Curr Top Med Chem* 5:539–546.
14. Staats PS, Hekmat H, Staats AW (2004) The psychological behaviorism theory of pain and the placebo: Its principles and results of research application. *Adv Psychosom Med* 25:28–40.
15. Bauer CS, et al. (2009) The increased trafficking of the calcium channel subunit alpha2delta-1 to presynaptic terminals in neuropathic pain is inhibited by the alpha2delta ligand pregabalin. *J Neurosci* 29:4076–4088.
16. Zamponi GW, Striessnig J, Koschak A, Dolphin AC (2015) The physiology, pathology, and pharmacology of voltage-gated calcium channels and their future therapeutic potential. *Pharmacol Rev* 67:821–870.
17. Perez-Pinzon MA, Yenari MA, Sun GH, Kunis DM, Steinberg GK (1997) SNX-111, a novel, presynaptic N-type calcium channel antagonist, is neuroprotective against focal cerebral ischemia in rabbits. *J Neurol Sci* 153:25–31.
18. Dolphin AC (2009) Calcium channel diversity: Multiple roles of calcium channel subunits. *Curr Opin Neurobiol* 19:237–244.
19. Richards MW, Butcher AJ, Dolphin AC (2004) Ca2+ channel beta-subunits: Structural insights AID our understanding. *Trends Pharmacol Sci* 25:626–632.
20. Van Petegem F, Clark KA, Chatelain FC, Minor DL, Jr (2004) Structure of a complex between a voltage-gated calcium channel beta-subunit and an alpha-subunit domain. *Nature* 429:671–675.
21. Bell DC, et al. (2001) Biophysical properties, pharmacology, and modulation of human, neuronal L-type (alpha(1D), Ca(V)1.3) voltage-dependent calcium currents. *J Neurophysiol* 85:816–827.
22. Van Petegem F, Duderstadt KE, Clark KA, Wang M, Minor DL, Jr (2008) Alanine-scanning mutagenesis defines a conserved energetic hotspot in the CaValpha1 AID-CaVbeta interaction site that is critical for channel modulation. *Structure* 16:280–294.
23. Butcher AJ, Leroy J, Richards MW, Pratt WS, Dolphin AC (2006) The importance of occupancy rather than affinity of CaV(beta) subunits for the calcium channel I-II linker in relation to calcium channel function. *J Physiol* 574:387–398.
24. Opatowsky Y, Chomsky-Hecht O, Kang MG, Campbell KP, Hirsch JA (2003) The voltage-dependent calcium channel beta subunit contains two stable interacting domains. *J Biol Chem* 278:52323–52332.
25. Cantí C, et al. (2001) Evidence for two concentration-dependent processes for beta-subunit effects on alpha1B calcium channels. *Biophys J* 81:1439–1451.
26. Cukuroglu E, Engin HB, Gursoy A, Keskin O (2014) Hot spots in protein-protein interfaces: Towards drug discovery. *Prog Biophys Mol Biol* 116:165–173.
27. Kortemme T, Baker D (2002) A simple physical model for binding energy hot spots in protein-protein complexes. *Proc Natl Acad Sci USA* 99:14116–14121.
28. Clackson T, Wells JA (1995) A hot spot of binding energy in a hormone-receptor interface. *Science* 267:383–386.
29. Keskin O, Ma B, Nussinov R (2005) Hot regions in protein–Protein interactions: The organization and contribution of structurally conserved hot spot residues. *J Mol Biol* 345:1281–1294.
30. Bogan AA, Thorn KS (1998) Anatomy of hot spots in protein interfaces. *J Mol Biol* 280:1–9.
31. Gohlke H, Kiel C, Case DA (2003) Insights into protein-protein binding by binding free energy calculation and free energy decomposition for the Ras-Raf and Ras-RalGDS complexes. *J Mol Biol* 330:891–913.
32. Metz A, et al. (2012) Hot spots and transient pockets: Predicting the determinants of small-molecule binding to a protein-protein interface. *J Chem Inf Model* 52:120–133.
33. Wells JA, McClendon CL (2007) Reaching for high-hanging fruit in drug discovery at protein-protein interfaces. *Nature* 450:1001–1009.
34. Pelay-Gimeno M, Glas A, Koch O, Grossmann TN (2015) Structure-based design of inhibitors of protein-protein interactions: Mimicking peptide binding epitopes. *Angew Chem Int Ed Engl* 54:8896–8927.
35. Laraia L, McKenzie G, Spring DR, Venkitaraman AR, Huggins DJ (2015) Overcoming chemical, biological, and computational challenges in the development of inhibitors targeting protein-protein interactions. *Chem Biol* 22:689–703.
36. Arkin MR, Tang Y, Wells JA (2014) Small-molecule inhibitors of protein-protein interactions: Progressing toward the reality. *Chem Biol* 21:1102–1114.
37. Aeluri M, et al. (2014) Small molecule modulators of protein-protein interactions: Selected case studies. *Chem Rev* 114:4640–4694.
38. Thompson AD, Dugan A, Gestwicki JE, Mapp AK (2012) Fine-tuning multiprotein complexes using small molecules. *ACS Chem Biol* 7:1311–1320.
39. Watkins AM, Arora PS (2015) Structure-based inhibition of protein-protein interactions. *Eur J Med Chem* 94:480–488.
40. Azzarito V, Long K, Murphy NS, Wilson AJ (2013) Inhibition of α-helix-mediated protein-protein interactions using designed molecules. *Nat Chem* 5:161–173.
41. Petros AM, et al. (2006) Discovery of a potent inhibitor of the antiapoptotic protein Bcl-xL from NMR and parallel synthesis. *J Med Chem* 49:656–663.
42. Wilson CG, Arkin MR (2011) Small-molecule inhibitors of IL-2/IL-2R: Lessons learned and applied. *Curr Top Microbiol Immunol* 348:25–59.
43. Zhao Y, Aguilar A, Bernard D, Wang S (2015) Small-molecule inhibitors of the MDM2-p53 protein-protein interaction (MDM2 inhibitors) in clinical trials for cancer treatment. *J Med Chem* 58:1038–1052.
44. Halgren T (2007) New method for fast and accurate binding-site identification and analysis. *Chem Biol Drug Des* 69:146–148.
45. Xu D, Jalal SI, Sledge GW, Meroueh SO (2016) Small-molecule binding sites to explore protein-protein interactions in the cancer proteome. *Mol Biosyst* 12:3067–3087.
46. Khanna M, et al. (2011) Targeting multiple conformations leads to small molecule inhibitors of the uPAR·uPA protein-protein interaction that block cancer cell invasion. *ACS Chem Biol* 6:1232–1243.
47. Rullo AF, et al. (2016) Re-engineering the immune response to metastatic cancer: Antibody-recruiting small molecules targeting the urokinase receptor. *Angew Chem Int Ed Engl* 55:3642–3646.
48. Konopleva M, et al. (2006) Mechanisms of apoptosis sensitivity and resistance to the BH3 mimetic ABT-737 in acute myeloid leukemia. *Cancer Cell* 10:375–388.
49. Jerabek-Willemsen M, Wienken CJ, Braun D, Baaske P, Duhr S (2011) Molecular interaction studies using microscale thermophoresis. *Assay Drug Dev Technol* 9:342–353.
50. Seidel SA, et al. (2012) Label-free microscale thermophoresis discriminates sites and affinity of protein-ligand binding. *Angew Chem Int Ed Engl* 51:10656–10659.
51. Yasuda T, Lewis RJ, Adams DJ (2004) Overexpressed Ca(v)beta3 inhibits N-type (Cav2.2) calcium channel currents through a hyperpolarizing shift of ultra-slow and closed-state inactivation. *J Gen Physiol* 123:401–416.
52. Buraei Z, Yang J (2013) Structure and function of the β subunit of voltage-gated Ca^{2+} channels. *Biochim Biophys Acta* 1828:1530–1540.
53. Feldman P, Due MR, Ripsch MS, Khanna R, White FA (2012) The persistent release of HMGB1 contributes to tactile hyperalgesia in a rodent model of neuropathic pain. *J Neuroinflammation* 9:180.
54. Due MR, et al. (2014) Carbamazepine potentiates the effectiveness of morphine in a rodent model of neuropathic pain. *PLoS One* 9:e107399.
55. Heblich F, Tran Van Minh A, Hendrich J, Watschinger K, Dolphin AC (2008) Time course and specificity of the pharmacological disruption of the trafficking of voltage-gated calcium channels by gabapentin. *Channels (Austin)* 2:4–9.
56. Bernstein GM, Jones OT (2007) Kinetics of internalization and degradation of N-type voltage-gated calcium channels: Role of the alpha2/delta subunit. *Cell Calcium* 41:27–40.
57. Lai J, Porreca F, Hunter JC, Gold MS (2004) Voltage-gated sodium channels and hyperalgesia. *Annu Rev Pharmacol Toxicol* 44:371–397.
58. Berman HM, et al. (2000) The protein data bank. *Nucleic Acids Res* 28:235–242.
59. Word JM, Lovell SC, Richardson JS, Richardson DC (1999) Asparagine and glutamine: Using hydrogen atom contacts in the choice of side-chain amide orientation. *J Mol Biol* 285:1735–1747.
60. Sanner MF (2005) A component-based software environment for visualizing large macromolecular assemblies. *Structure* 13:447–462.
61. Lin Y, McDonough SI, Lipscombe D (2004) Alternative splicing in the voltage-sensing region of N-Type CaV2.2 channels modulates channel kinetics. *J Neurophysiol* 92:2820–2830.
62. Chen X, et al. (2017) Molecular determinants of the sensitivity to Gq/11-phospholipase C-dependent gating, Gd^{3+} potentiation, and Ca^{2+} permeability in the transient receptor potential canonical type 5 (TRPC5) channel. *J Biol Chem* 292:898–911.
63. Chakraborty S, et al. (2011) Bromoenol lactone inhibits voltage-gated Ca^{2+} and transient receptor potential canonical channels. *J Pharmacol Exp Ther* 339:329–340.
64. National Research Council (2011) *Guide for the Care and Use of Laboratory Animals* (National Academies Press, Washington, DC), 8th Ed.
65. Xie JY, et al. (2016) Sustained relief of ongoing experimental neuropathic pain by a CRMP2 peptide aptamer with low abuse potential. *Pain* 157:2124–2140.
66. Bhangoo S, et al. (2007) Delayed functional expression of neuronal chemokine receptors following focal nerve demyelination in the rat: A mechanism for the development of chronic sensitization of peripheral nociceptors. *Mol Pain* 3:38.

BIOCHEMISTRY